Electronic materials

Optimisation of processing conditions during CVD growth of 2D WS$_2$ films from a chloride precursor

William R. Campbell[1,2,*] , Francesco Reale[2], Ravi Sundaram[2], and Simon J. Bending[1]

[1] Centre for Nanoscience and Nanotechnology, University of Bath, Claverton Down, Bath BA2 7AY, UK
[2] Oxford Instruments Plasma Technology, North End, Yatton, Bristol BS49 4AP, UK

ABSTRACT

Monolayer tungsten disulphide (WS$_2$) is a direct band gap semiconductor which holds promise for a wide range of optoelectronic applications. The large-area growth of WS$_2$ has previously been successfully achieved using a W(CO)$_6$ precursor, however, this is flammable and a potent source of carbon monoxide (CO) upon decomposition. To address this issue, we have developed a process for the wafer-scale growth of monolayer WS$_2$ from a tungsten hexachloride (WCl$_6$) precursor in a commercial cold-wall CVD reactor. In comparison to W(CO)$_6$, WCl$_6$ is less toxic and less reactive and so lends itself better to the large-scale CVD growth of 2D layers. We demonstrate that a post-growth H$_2$S anneal can lead to a dramatic improvement in the optical quality of our films as confirmed by photoluminescence (PL) and Raman measurements. Optimised films exhibit PL exciton emission peaks with full width at half maximum of 51 ± 2 meV, comparable to other state-of-the-art methods. We demonstrate that our WS$_2$ films can be readily transferred from the sapphire growth substrate to a Si/SiO$_2$ target substrate with no detectable degradation in quality using a polystyrene support layer. Our approach represents a promising step towards the industrial-scale fabrication of p-n junctions, photodetectors and transistors based on monolayer WS$_2$.

Introduction

Semiconducting transition metal dichalcogenides (TMDs) have attracted growing interest over the last decade due to the unique physical properties they exhibit when reduced from a bulk crystal to a monolayer [1–3]. In bulk form, the transition metal disulphides and diselenides (MoS$_2$, WS$_2$, WSe$_2$ and MoSe$_2$) are indirect semiconductors with a valance band maximum located at the Γ point, whereas in monolayer form they possess direct band gaps with

both the conduction band minimum and valence band maximum at the K point [4]. Monolayer tungsten disulphide (WS$_2$) is one of the most widely investigated members of the family of semiconducting Group VI TMDs due to its direct band gap of 2 eV [5], very high carrier mobility [6] and superior optical quality [7–9] in comparison with its molybdenum-based counterparts. Potential applications of WS$_2$ range from light-emitting diodes (LEDs) [10, 11], photodetectors [12–14], valley-electronics [15, 16] and field-effect transistors [17–19]. Achieving high-quality large-area monolayer WS$_2$ films remains a major challenge. If this material is to make the transition from proof-of-principle laboratory research to industrial applications, sustainable growth methods must be developed that produce large-area films on an industrial scale, without sacrificing the material quality.

Chemical vapour deposition (CVD) is the technique of choice for the growth of large-area WS$_2$ films due to its compatibility with both monolayer deposition and industrial scalability. Over the last decade, major efforts have been devoted worldwide to developing various CVD approaches for monolayer WS$_2$ growth. Solid powder tungsten oxide (WO$_3$) has been extensively studied as a tungsten CVD growth precursor [8, 20, 21] with very promising results. WO$_3$ has been chosen primarily because of its low toxicity when compared to the organic and halide precursors, as well as the effective replacement of O by S in the CVD reaction [22]. WS$_2$ crystals grown by this method have been shown to form with high crystallinity [21], excellent optical properties, e.g. photoluminescence linewidths comparable to pristine exfoliated WS$_2$ monolayer flakes [7, 20, 23], and reasonable carrier mobilities [20]. However, powder-based CVD methods are challenging to scale up to large-area industrial production levels since they usually represent 'single shot' processes. The random nature of seeding and nucleation on common growth substrates also typically leads to large individual WS$_2$ domains [24, 25] rather than the uniform layers that are ideally required. In addition to solid powder precursors, there has also been a lot of interest in gas-source CVD of WS$_2$ films [26–29]. The greatest advantage with this approach is that gas flow rates can be precisely controlled using mass flow controllers (MFCs), allowing for far greater reproducibility and much greater flexibility in the choice of tungsten precursor [30]. One common example of the latter is tungsten hexacarbonyl, W(CO)$_6$, a hexacarbonyl metal precursor that is stable in air, it is a solid at room temperature and decomposes at temperatures between 600 and 900 °C in the presence of H$_2$ [31–33]. Using W(CO)$_6$ as a precursor Kang et al. have reported the growth of continuous monolayer WS$_2$ films with grain sizes of $\sim$ 1 μm on 4-inch fused silica substrates that exhibited carrier mobilities of 18 cm^2/V-s [34]. However, the reported growth times of up to 26 h were very long and the diethyl sulphide (DES) sulphur source used has been demonstrated to lead to carbon contamination of the films [35]. The latter gives rise to partial quenching of the WS$_2$ photoluminescence (PL) and can also detrimentally affect its electronic properties [27, 35].

Tungsten halide precursors have also been widely investigated [26, 29, 36–38] due to their relatively low decomposition temperatures and the absence of hydrocarbon reaction products which could incorporate as impurities. In this paper, we describe investigations of the growth of WS$_2$ on c-plane sapphire using the metal halide WCl$_6$ as the tungsten source in a cold-wall CVD reactor. We employ argon (Ar) as the WCl$_6$ carrier gas and hydrogen sulphide (H$_2$S) as the sulphur source. There are several reasons why we have chosen WCl$_6$ as our W precursor. Firstly, unlike a metal-organic precursor such as tungsten hexacarbonyl (W(CO)$_6$), WCl$_6$ and H$_2$S cannot create any hydrocarbon reaction products that could lead to carbon incorporation in the WS$_2$ films. Carbon contamination is known to partially quench the photoluminescence and lead to the growth of poor-stoichiometry WS$_2$ which is more susceptible to oxidation [27]. Secondly, metal halide precursors have been used by the microelectronics industry for decades [39–41] and have high enough vapour pressures at reasonable temperatures to be employed in a CVD reactor. On the downside, WCl$_6$ decomposition produces hydrogen chloride (HCl), and WCl$_6$ itself is an aggressive oxidant, so correct and safe containment is needed. This containment is also necessary to prevent exposure to skin and the eyes as WCl$_6$ can cause skin corrosion and eye damage, as well as to prevent inhalation as WCl$_6$ can cause specific organ toxicity. The HCl by-product is removed via the chamber outflow system. In practice, we selected WCl$_6$ over tungsten hexafluoride (WF$_6$) as the HF reaction product is far more corrosive than the HCl released during growth from WCl$_6$. HCl is also much more volatile than HF at typical growth temperatures

resulting in negligible chloride contamination of our films (see Supplementary materials).

All process gases flowing into our cold-wall CVD reactor could be precisely controlled via mass-flow controllers, allowing systematic studies to be performed in order to optimise gas flow rates and pressures as well as process temperatures and times. We have also investigated how a post-growth hydrogen sulphide anneal affects the optical quality of the as-grown WS_2 films. Using wafer delivery through a load lock, we achieve total growth process times of approximately 40 min, from loading to unloading. The load lock also allows us to keep the growth chamber under vacuum and the wafer stage close to its growth temperature. Finally, we demonstrate that our films are easy to transfer from the sapphire growth substrate to a target substrate, such as Si/SiO_2, using a polystyrene supporting membrane and release in water.

Material and methods

The synthesis of WS_2 was carried out via gas-phase chemical vapour deposition in an Oxford Instruments Nanofab cold-wall CVD reactor using WCl_6 and H_2S as the W and S sources, respectively. A schematic of the main components of the growth system can be seen in Fig. 1. The WCl_6 precursor was kept at 90 °C in a stainless-steel bubbler to establish a sufficiently high vapour pressure and transported to the reaction chamber with Ar carrier gas. We also incorporate a small amount of H_2 to promote WS_2 growth. Firstly, it has been reported that hydrogen can act as a chemical etchant which leads to a decrease in nucleation density [42, 43]. A lower nucleation density can lead to larger domain sizes and less grain boundaries, increasing the material quality. Secondly, and crucially, the addition of hydrogen during synthesis accelerates the efficient reduction of the tungsten precursor WCl_6 that has an oxidation state of $+6$ and needs to be in a $+4$ state to form WS_2. Hydrogen aids this reduction process and thus promotes the conversion of the tungsten precursor to WS_2 [44].

In practice, our process was operated at a growth temperature of 600 °C and a total growth pressure of 4.5 Torr. The H_2 flow was kept constant at 10sccm during all growths, whereas the H_2S flow was varied between them to investigate its role, e.g. in the formation of sulphur vacancies in the WS_2 films.

C-plane (0001) surface orientation sapphire wafers were the substrates of choice for the synthesis of WS_2 monolayer films, although growth on Si/SiO_2 has also been successfully achieved. Sapphire was used due to its atomically flat surface which leads to a lower nucleation density and thus a higher-quality growth. The crystal lattice of sapphire (4.785 Å) is also $\sim 50\%$ larger than WS_2 (3.153 Å), which allows for the formation of a 3:2 superstructure of WS_2. This commensurability of the sapphire lattice with the WS_2 lattice allows for Van der Waals interactions to control the orientation of the WS_2 film [45]. This preferential orientation leads to a reduction in the

Figure 1 Schematic of the Oxford Instruments Nanofab CVD reactor used for WS_2 monolayer synthesis. MFCs are the mass flow controllers used to control the gas flow rates.
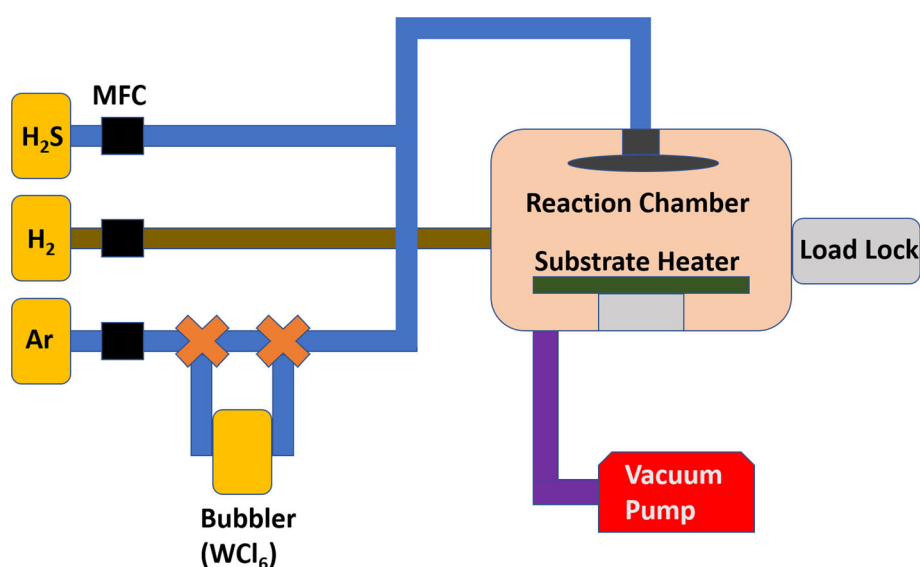
number of grain boundaries and an overall increase in film quality [45].

The primary process optimisation revolved around investigating the effect of a post-growth H_2S anneal, and how different flow rates of this gas affected the final WS_2 film quality. Raman and photoluminescence (PL) spectroscopy were used to characterise the optical quality of the WS_2 while atomic force microscopy (AFM) was used to measure its thickness. All Raman and PL measurements were made using a Renishaw inVia microscope at room temperature and under ambient atmospheric conditions with an excitation wavelength of 532 nm.

Results and discussion

Successful growth on a 2-inch C-plane sapphire substrate was performed at 600 °C for 15 min in a 4.5 Torr total pressure with Ar, H_2S and H_2 flow rates of 100, 10 and 10sccm, respectively. The Raman spectrum from a typical sample grown under these conditions is shown in Fig. 2a.

In Fig. 2a, we observe the three main WS_2 peaks of interest, the E^1_{2g}, A_{1g} and 2LA(M) [46]. The in-plane phonon mode E^1_{2g} and the out-of-plane phonon mode A_{1g} peaks are first-order Raman modes, whereas the 2LA(M) is a second-order Raman mode that is activated by disorder [46]. It is reported in the literature that these three Raman peaks will shift as the layer thickness is reduced [23, 46–48]. The A_{1g} peak redshifts, whereas the 2LA and E^1_{2g} peaks slightly blue shift, and Berkdemir et al. demonstrate that a separation between the A_{1g} and E^1_{2g} of 62 cm^{-1} is indicative of a WS_2 monolayer [46, 48–50]. For the

spectrum of Fig. 2a, we extract the A_{1g} peak position to be 418.4 cm^{-1} and the E^1_{2g} peak position to be 356.2 cm^{-1}, yielding a peak separation of 62.2 cm^{-1}, in good agreement with this estimate for monolayer films. AFM measurements also confirmed that this was a monolayer film which we would expect to have a direct band gap and exhibit strong photoluminescence [8, 20, 23, 49]. However, in practice, we only observed a very weak PL signal as shown in Fig. 2b. For comparison, high-quality monolayer samples produced by mechanical exfoliation typically exhibit a PL signal with a narrow full width at half maximum (40-60 meV) [20, 51] centred on ∼ 2.0 eV. This observation could be attributed to a sulphur deficiency in the films deposited under these process conditions. This conclusion is supported by reports from both chemical vapour transport (CVT) crystal growth of TMDs and CVD growth utilising $W(CO)_6$ as the W source [8, 20, 52]. In the case of CVT growth, studies have shown that the materials suffer from a natural chalcogen deficiency due to the volatility of the chalcogen atoms [53, 54]. To alleviate this, CVT-produced TMDs are deliberately grown with a stoichiometric ratio greater than 2:1 (chalcogen: metal). Similarly, sulphur vacancies are frequently observed in CVD-grown TMDs [55]. It is generally accepted that these defects introduce charge traps and accelerate electron–hole recombination, and ab initio quantum dynamics calculations by Li et al. have specifically implicated sulphur vacancies as being responsible for accelerating non-radiative charge carrier recombination [56].

Several works have reported that a post-growth anneal in a sulphur atmosphere can lead to an
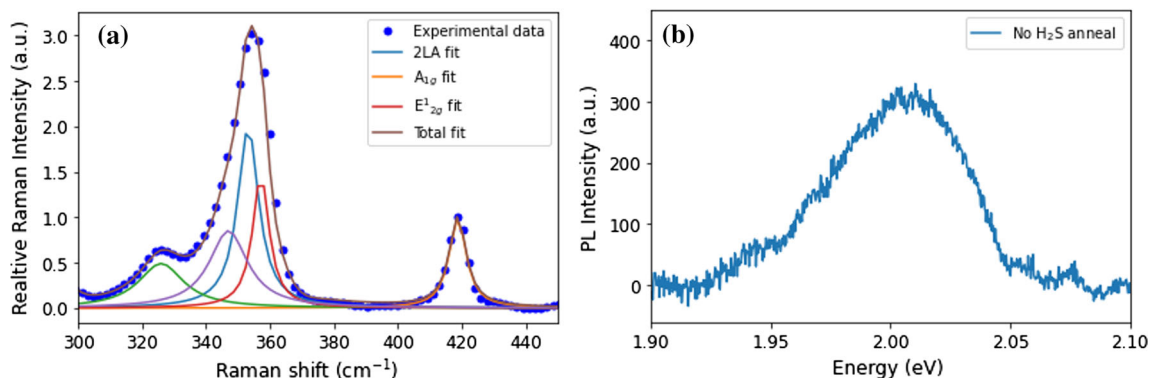

Figure 2 **a** Typical Raman spectrum (normalised to the A_{1g} peak) of a WS_2 film grown with 100sccm Ar, 10sccm H_2S, and 10sccm H_2. The peaks have been distinguished by Lorentzian fitting to show how each Raman mode contributes to the overall spectrum, **b** weak PL spectrum observed from a WS_2 growth with no post-growth anneal.

Figure 3 **a** Raman spectra of the four annealing tests (10sccm, 20sccm, 30sccm, 40sccm H_2S). Lorentzian functions have been fitted to the peaks to extract the contribution of each Raman mode, **b** PL spectra of the four annealing tests. Gaussian functions have been fitted to the PL peaks to extract the excitonic and trionic contributions to the overall PL spectra. Both the Raman and PL spectra are normalised to the A_{1g} peak.
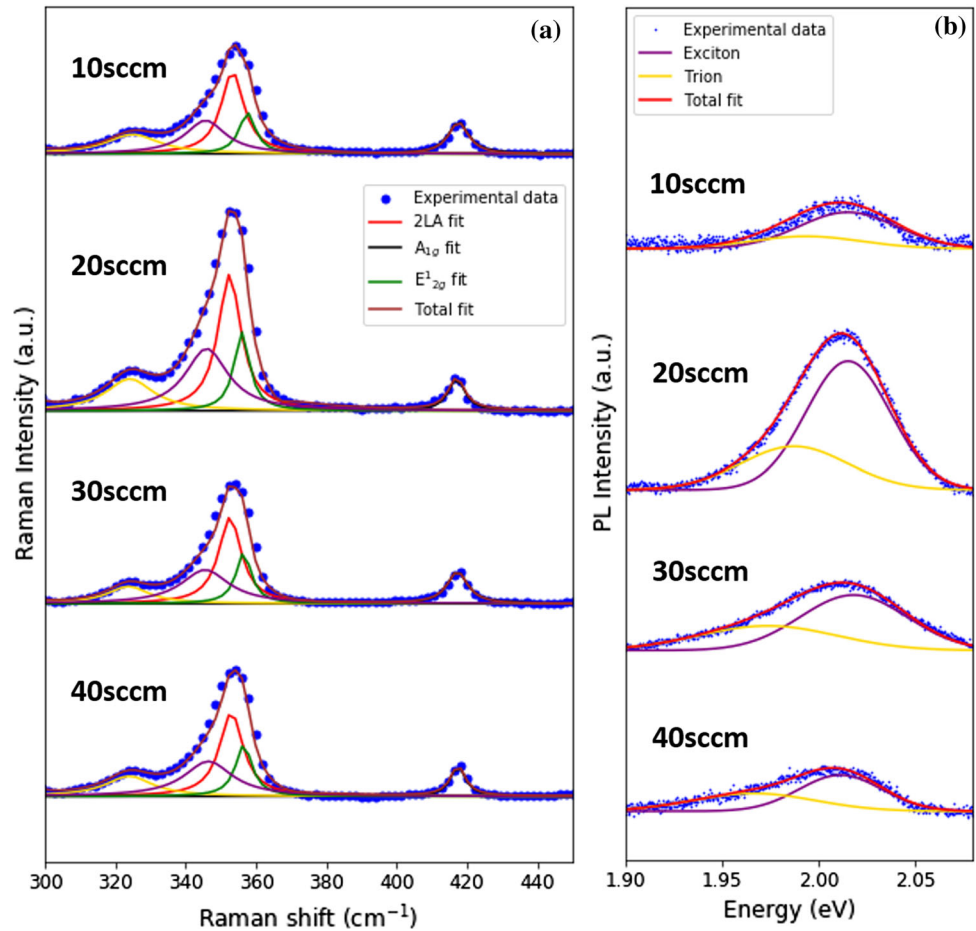
increase in the optical quality of MoS_2 and WS_2 thin films [7, 47, 57]. With this in mind, we have performed additional growth runs that incorporated a post-growth H_2S anneal with flow rates ranging from 10 to 40 sccm. All growths were performed at 600 °C and a total pressure of 4.5 Torr. Annealing was carried out at 600 °C and a total pressure of 4.5 Torr and lasted for 15 min. The anneal immediately followed the growth stage whereby the H_2 and Ar were switched off and the H_2S continued to flow. The parameters during the initial growth stage are the same as those described above.

Upon examining the Raman spectra for the growth runs shown in Fig. 3a, we find that the A_{1g} and E^1_{2g} peak separations remained constant for all films at $\sim 62 \text{ cm}^{-1}$, indicating that all the locations where the WS_2 films were measured represent monolayers [46]. However, clear patterns emerge in Fig. 3a and b which provide evidence for a change in material quality when the H_2S flow rate is varied. We can extract several key figures-of-merit from the Raman

spectra of Fig. 3a by fitting multiple Lorentzian functions to isolate each peak of interest [46]. These are the full width at half maximum (FWHM) values of the 2LA, E^1_{2g} and A_{1g} peaks and the $A_{1g}/2LA$ and A_{1g}/E^1_{2g} peak intensity ratios. We find that the ratio of the 2LA and A_{1g} ($A_{1g}/2LA$) peak heights initially decreases as the H_2S flow rate during the anneal is increased from 10 to 20sccm and then increases again up to 40sccm, as shown in Fig. 4a. This trend is also clearly visible in the A_{1g}/E^1_{2g} ratio on the same figure.

In our case both E^1_{2g} and A_{1g} Raman peak separations and AFM measurements confirm that the regions of WS_2 that were measured are of monolayer thickness and the same substrate (sapphire) and laser wavelength (532 nm) is used throughout all measurements, allowing us to exclude possible changes in film thickness. These changes in peak ratio are also correlated with changes in the FWHMs of the three peaks of interest as shown in Fig. 4b. Across all growth runs, the peak FWHM remained close to 8.0
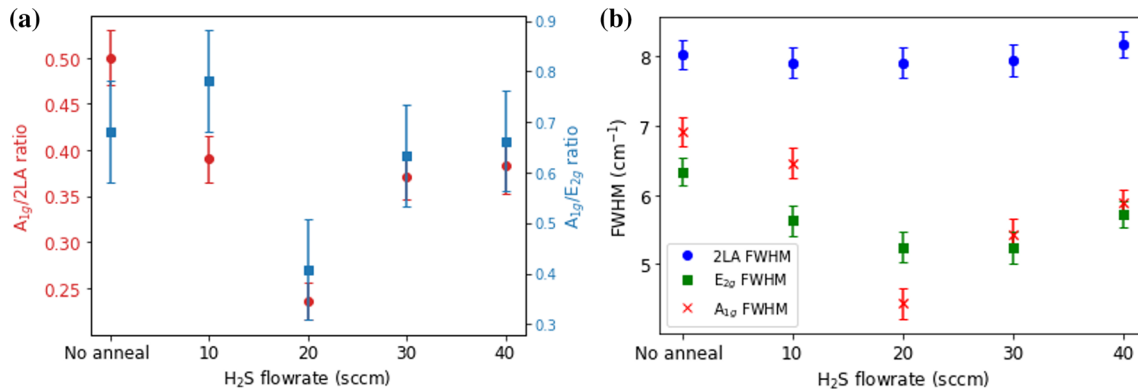
Figure 4 a Peak intensity ratios **b** and FWHM values extracted from the Raman spectra of Fig. 3a. From the exhibited trends we infer that the optimal films are grown at H_2S flow rates close to 20sccm during the annealing phase.

cm^{-1} but reached its lowest value of 7.90 cm^{-1} at the 10sccm and 20sccm H_2S flow rates. However, the FWHMs of the E^1_{2g} and the A_{1g} peaks were lower in the 20sccm H_2S sample, suggesting an improvement in crystalline quality when compared to samples without a post-growth anneal [52, 58–61]. We also find that increasing the H_2S flow rate to 30sccm and 40sccm during the anneal has a detrimental effect on the E^1_{2g} and A_{1g} FWHMs. A possible cause of this could be the formation of defects caused by etching due to the increased amount of hydrogen. This observation suggests that annealing conditions, if not carefully chosen, can result in poorer quality of the resulting WS_2.

Using tip-enhanced resonance Raman scattering (TERS), Chanwoo Lee *et. al.* [62] have shown that both the 2LA(M) and the A_{1g} Raman peaks depend on the density of structural defects in WS_2, specifically the number of sulphur vacancies (V_S). They observe a red shift of the A_{1g} peak with increasing V_S as well as a broadening of its FWHM due to the asymmetric D peak splitting off on the low-energy side. The 2LA(M) peak is also found to reduce in intensity with increasing density of sulphur vacancies. We believe we observe the same trend in the films that we assign to be of a lesser quality. In their paper, Chanwoo Lee et al. [62] show that there is an anti-correlation between the amplitude of the D peak (which grows with defect density) and the A_{1g} peak. They also show that the amplitudes of the 2LA(M) and A_{1g} are correlated, though are unable to determine the functional form of the relationship between them. Our observed decrease in the A_{1g} FWHM as we quench sulphur vacancies under

optimum annealing conditions is fully consistent with this scenario.

Figure 3b shows the results of a study of the PL as a function of H_2S flow to determine optimal annealing conditions.

One direct measure of the crystalline quality of WS_2 is the full width at half-maximum (FWHM) of the PL exciton peaks [50]. To investigate this, we fit Gaussian curves to the PL data of Fig. 3b which allows us to individually quantify the exciton and trion contributions and calculate their peak ratios. These are displayed in Fig. 5 and mirror the changes observed in the Raman spectra. Firstly, the exciton/trion intensity ratio (Fig. 5a) reflects the same trend as the A_{1g}/2LA peak intensity ratios shown in Fig. 4a, rising to a maximum for a 20sccm H_2S anneal and falling again at higher H_2S flow rates. The normalised amplitude of both exciton and trion peaks increases at 20sccm reflecting an overall reduction in non-radiative recombination which we attribute to a reduction in the density of S vacancies [20, 55, 56, 63]. The observation that the peak ratio is a maximum after a 20sccm H_2S anneal also indicates a suppression of the trion peak relative to the exciton PL peak, suggesting an additional decrease in the extrinsic electron density [8, 20, 63, 64]. Further evidence for an increase in the crystalline quality comes from the extracted exciton PL FWHM values shown in Fig. 5b and again the lowest FWHM is measured in the sample annealed in 20sccm H_2S. A lower PL FWHM is associated with an increase in material quality. As the FWHM increases, this indicates the emergence of some form of disorder in the material e.g. sulphur vacancies [50, 65, 66]. From this, we can infer that a
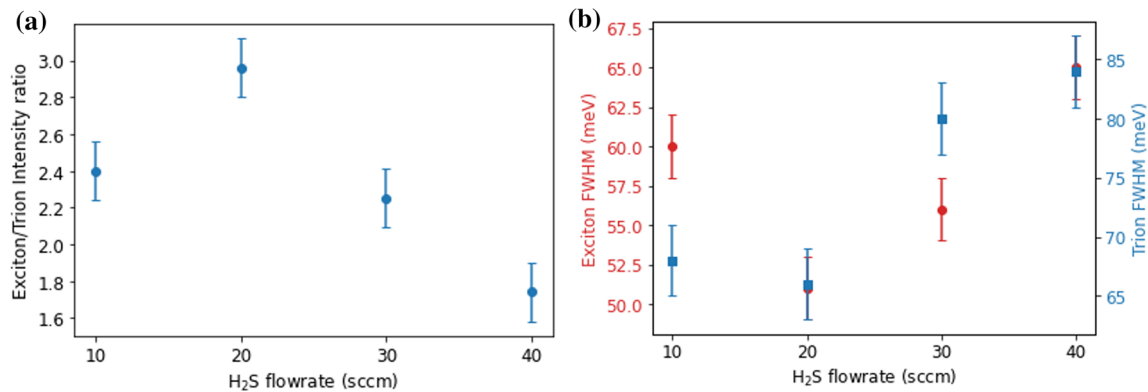
Figure 5 **a** PL exciton/trion peak ratios and **b** FWHM extracted from the PL data of Fig. 3b. This behaviour mirrors the trend seen in Fig. 4 and provides further confirmation that the 20sccm H_2S flow represents the optimum annealing conditions. Data for as- grown samples without an anneal have not been included here because their PL was completely dominated by the signal from the sapphire substrate.

20sccm H_2S anneal leads to a higher crystalline quality.

Based on the results of other published studies of the CVD growth and computational studies of MoS_2 [42, 56, 57, 67, 68] and WS_2 [63, 69] we believe that these PL intensity changes are associated with two competing processes. Firstly, as stated previously, the initial non-annealed sample almost certainly contains a high density of sulphur vacancies which facilitate non-radiative carrier recombination rather than the desired radiative recombination [56, 57, 63, 67–69]. The very large increase in PL intensity observed upon post-growth H_2S annealing suggests that it is quenching these sulphur vacancies by reconstruction of the as-grown layers, leading to much-improved material crystallinity. This picture is supported by the enhancements observed in the Raman peak ratios (c.f., Fig. 4a). In contrast, H_2S flow rates during annealing above 20sccm appear to be having a detrimental effect on both the Raman and PL spectra. This is most likely due to a second competing factor relating to the high abundance of H_2 [43]. At high temperatures, H_2S molecules readily dissociate to create a sulphur and hydrogen atmosphere. Hence, when the H_2S flowrate is increased above the apparent optimum of 20sccm there is now too much H_2 present, and the density of vacancy and other defects begins to increase again. Xiao et al. performed an in-depth study of the effects of hydrogen on MoS_2 atomic layers [42] and found that with increasing H_2 concentration, the energetically active H atoms were chemisorbed on the unstable S sites. This chemisorption leads to a breaking of the Mo-S bonds

at high temperature and thus a desulphurisation of the film. In TEM measurements on the same samples, they were able to observe circle-like defects that they identified as being sulphur vacancies. In practice, the microstructural damage caused to our films at high H_2S flow rates may originate from both desulphurisation as well as an oxidation-etching effect mediated by a greater presence of H_2 in the atmosphere [42, 43, 70].

Our best films exhibit an exciton FWHM of 51 ± 2 meV. When compared to WS_2 grown via powder-based methods [7, 20] and MOCVD [71], our FWHM is located at the upper end of values quoted in literature, which is to be expected. The advantage of WCl_6 compared to the powder-based method is much better scalability, and the advantage over the MOCVD films is the much shorter deposition time. FWHM values for films grown on sapphire substrates from a $W(CO)_6$ precursor range from 27 to 65 meV [27, 34, 70–72], and span 21-68 meV when WO_3 powder is used as a precursor [7, 20, 23, 73–75]. Our FWHM value is an improvement on values (67 meV) reported by Park et al. [26] who also employed gas-phase CVD with a WCl_6 precursor. Finally, comparing the FWHM for our best films to those grown from the tungsten halide WF_6 (exciton FWHM in the range 48–83 meV) [37, 38, 76] we find that our values fall closer to the lower end of reported values, with the added advantage that by using WCl_6 we eliminate the production of the much more corrosive reaction product, HF. Table S1 in supplementary materials presents a comprehensive comparison of key PL

Figure 6 **a** Map of the A_{1g} Raman peak position of WS_2 deposited on a 2-inch sapphire wafer indicating a high degree of uniformity across the sample, **b** Map of the PL intensity across the sample. The PL intensity remains uniform over most of the sample, **c** Map of the A_{1g} FWHM. This complements the A_{1g} peak position, also showing a high degree of uniformity across the sample, **d** Map of the exciton PL FWHM which further indicates a uniform WS_2 film.
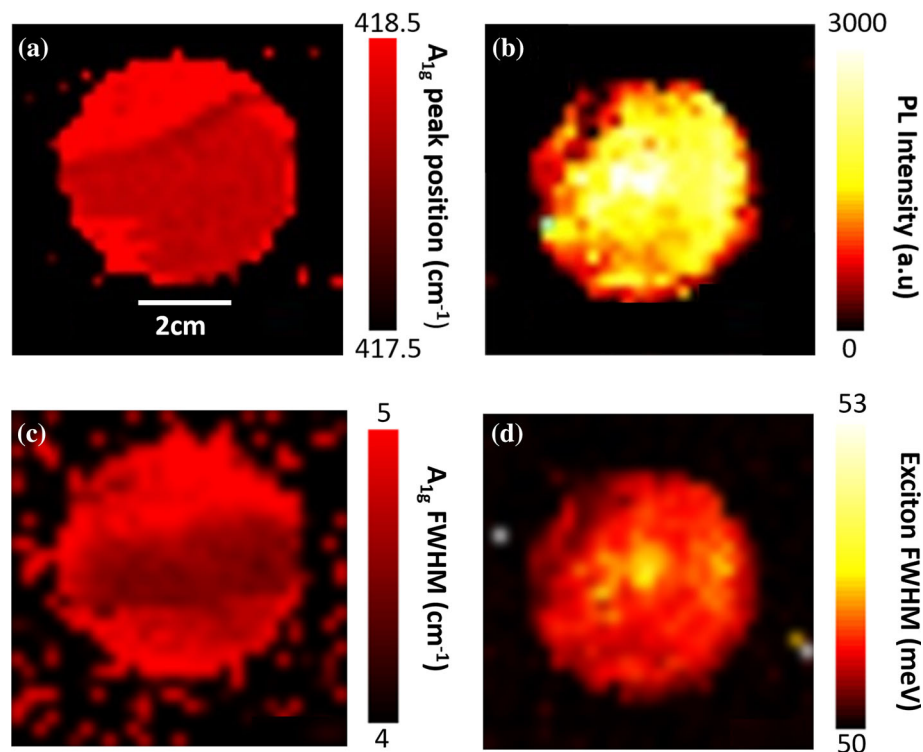
figures-of-merit for a range of different WS_2 growth methods and precursors.

For WS_2 to become a viable material for large-scale electronic and optoelectronic applications, it must be produced with high quality and uniformity on a suitably large scale [77, 78]. In Fig. 6, we show large-area Raman and PL maps of our optimal WS_2 films grown on C-plane sapphire to illustrate the homogeneous coverage our growth method can achieve. Figure 6a is a map of the A_{1g} Raman peak position. As we can see, the peak position remains constant at 418 ± 0.5 cm^{-1} across a vast majority of the 2-inch sample, indicating complete coverage and large-scale uniformity. Figure 6b is a map of the PL intensity and again shows a very uniform intensity over most of the sample, indicating a high level of optical uniformity. The drop-off in PL intensity near the edge of the sample is attributed to damage incurred during dicing and polishing of the wafer, leading to a much higher density of nucleation sites and more disordered or even amorphous areas of film in these regions. Figure 6c and 6d are maps of the A_{1g} FWHM and the exciton PL FWHM, respectively, that further show that we have a achieved a uniform film of WS_2.

Figure 7a displays a photograph of a typical WS_2 monolayer grown on a 2-inch sapphire wafer by our gas-phase CVD process at 600C and a total gas pressure of 4.5 Torr followed by an optimised 15-min H_2S anneal. The WS_2 film thickness was measured by AFM at the small scratch on the surface shown in the AFM image, Fig. 7b. The topographic line scan along the direction indicated in Fig. 7 reveals a film thickness of ~ 1.1 nm, consistent with the presence of a monolayer film [20, 21, 43].

In addition to being able to grow over large areas, it is also ideal to be able to transfer the WS_2 from sapphire to a Si/SiO_2 substrate in order to fabricate functional electronic and optoelectronic devices [79]. To achieve this, we have used the surface energy-assisted transfer process first described by Gurarslan et al. [79] which is shown diagrammatically in Fig. 8a. This method combines the benefits of a simple transfer protocol without harsh alkaline chemicals such as KOH, which can lead to film degradation [80]. The sample chosen for transfer was first spin-coated with a uniform layer of polystyrene (PS) dissolved in toluene at 3000 rpm for 60 s, followed immediately by a 15-min bake at 90C to harden the PS coating and promote adhesion. A few drops of deionised (DI) water were then dripped on top of the sample which was poked around the edges with a scalpel to create small perforations that allowed water to seep underneath the PS layer. As the sapphire substrate is hydrophilic and the WS_2

Figure 7 **a** Optical micrograph of a 2-inch sapphire wafer coated with a WS_2 grown using our optimised process, **b** AFM image of a small scratch in the WS_2 film which allows a determination of the film thickness, **c** topographic scan along the line indicated in **b** showing a thickness of $\sim$ 1.1 nm.
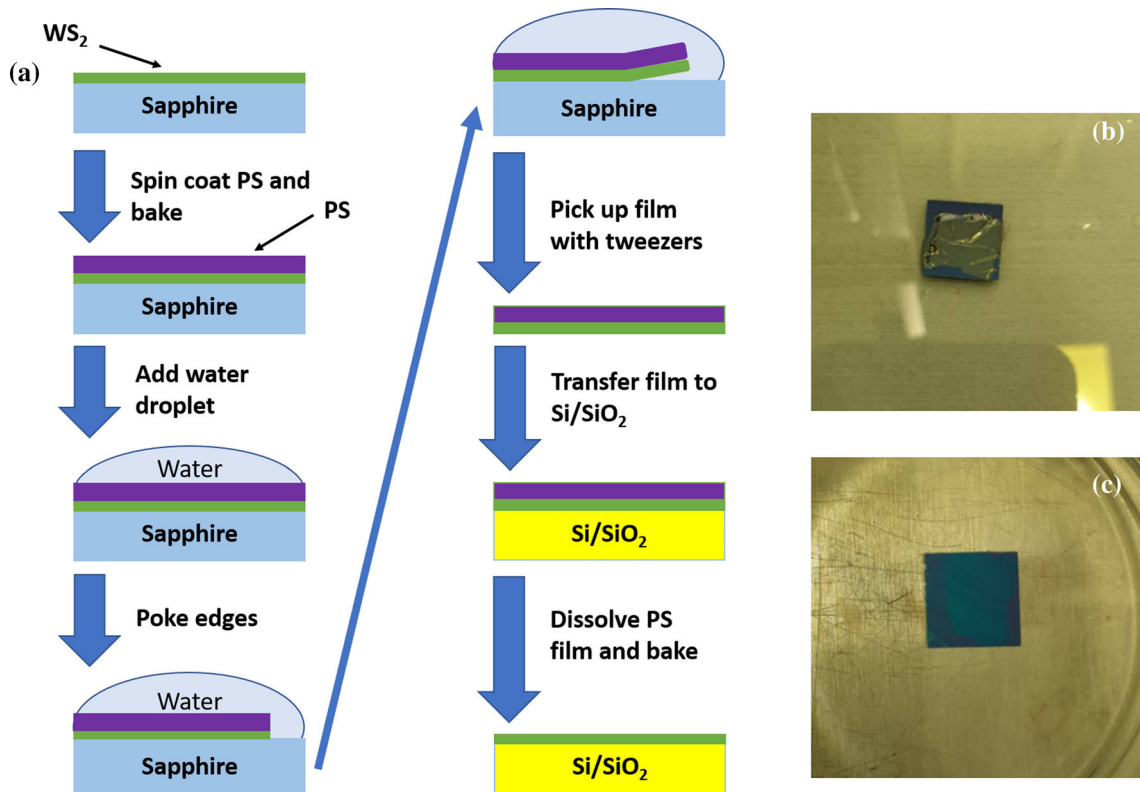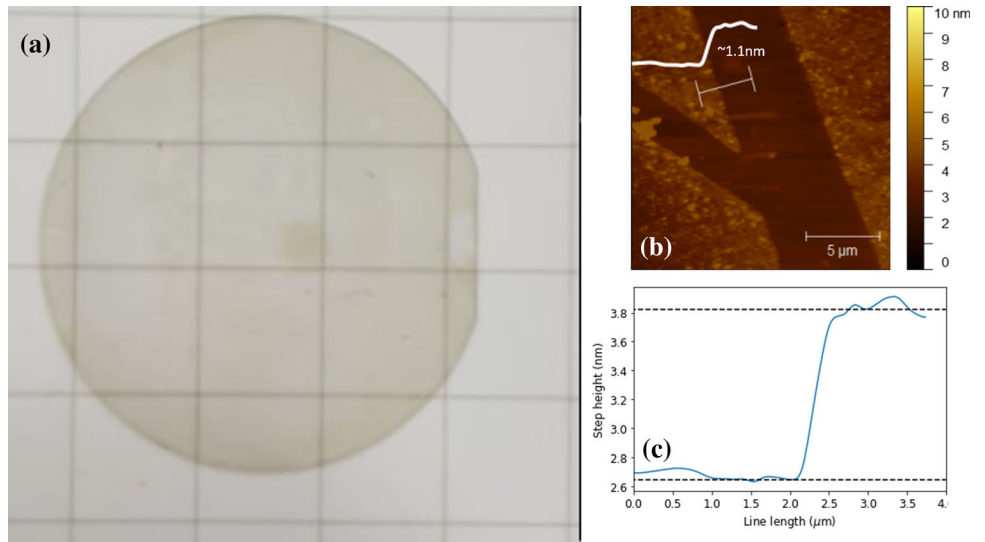

Figure 8 **a** Schematic diagram of the transfer protocol used for a WS_2 monolayer film grown on a sapphire substrate (adapted from Gurarslan et al. [78]). **b** The WS_2 film and PS layer when first transferred from the sapphire growth substrate to the Si/SiO$_2$ target substrate. **c** The WS_2 film post-baking to remove water and post-toluene soak to remove the PS layer.

hydrophobic [79], the water spread rapidly across the sapphire and delaminated the WS_2 film. Once it was floating freely in the water the film could be picked up with tweezers and placed onto a target substrate, as illustrated in Fig. 8b. The target substrate used was

an n^+-Si/SiO$_2$ wafer with a 300 nm thick oxide layer. The corner of a paper tissue was used to remove most of the water under the WS_2 film before it was baked at 80 °C for 1 h to remove most of the residual moisture. A second bake for 30 min at 150 °C was
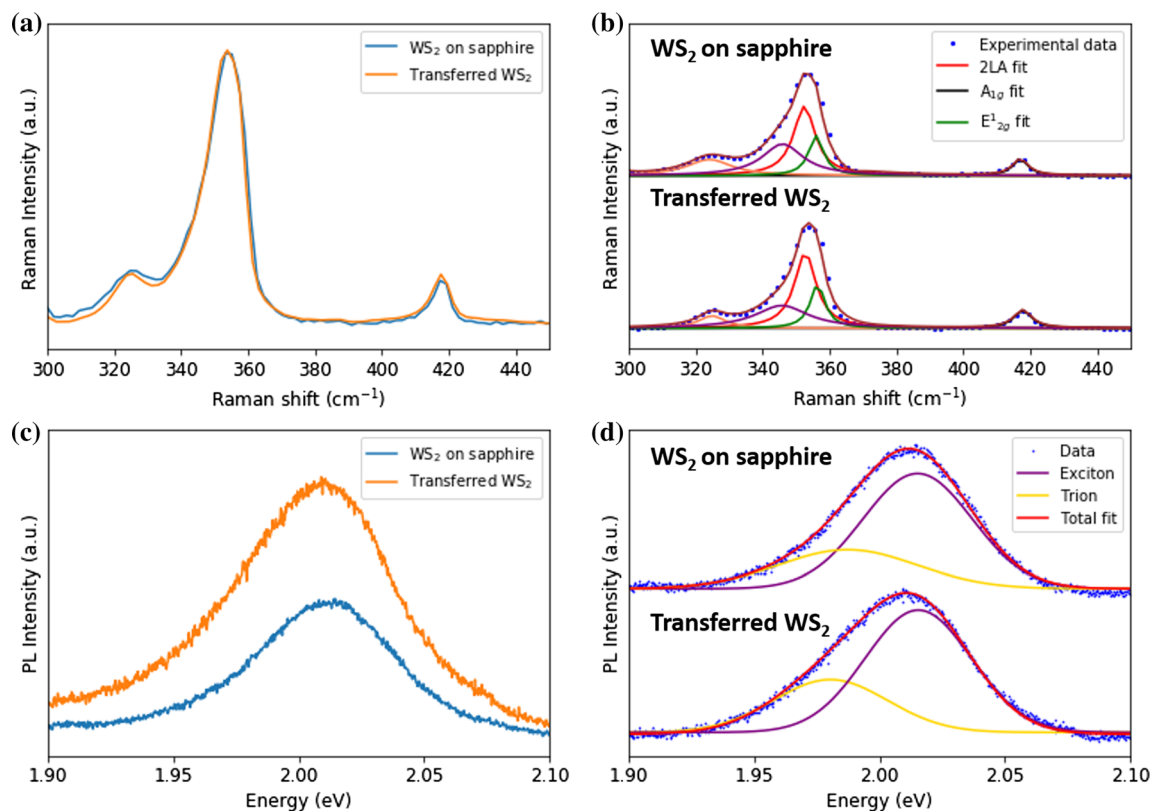
Figure 9 **a** Comparative Raman spectra (normalised to the A_{1g} peak) and **b** Lorentzian fits of the Raman spectra to extract the individual Raman peak contributions of the WS_2 monolayer pre- and post-transfer. Both **a** and **b** are normalised to the A_{1g} Raman mode. **c** Comparative PL spectra and **d** Gaussian fits of the PL spectra (normalised to the PL peak maximum) to extract the excitonic and trionic contributions.

then performed to spread the polymer and remove any remaining water. Finally, the PS layer was removed by soaking the sample in toluene for 1 h. A great advantage of this method is that after cleaning and annealing the sapphire substrate can be reused after transfer. This process is illustrated schematically in Fig. 8a, and an optical image of the film on the n^+-Si/SiO$_2$ chip post-transfer is shown in Fig. 8c.

Optical characterisation of the transferred films shows that their quality is well preserved, and that the transfer process has no detectable detrimental effect on the material. Figure 9a shows Raman spectra, normalised to the A_{1g} peak, of a film before and after transfer onto Si/SiO$_2$ exhibiting only a few very minor differences. Figure 9b shows the results of fitting Lorentzian peaks to these data revealing that there is actually a slight reduction in the FWHM of the 2LA peak from 7.90 to 7.80 cm^{-1}, which could be related to the release of strain after transfer [79, 81]. This interpretation is corroborated by a more careful analysis of the FWHM of the 325 cm^{-1} Raman mode

which was reduced by 42% from 17.12 cm^{-1} before transfer to 9.92 cm^{-1} afterwards. This effect has previously been observed by Dadgar et al. where they applied an external strain of 2.85% and observed a FWHM increase of 9.47% in the 325 cm^{-1} Raman peak [81]. Strain in the WS_2 film can arise due to the difference in the thermal expansion coefficients of the WS_2 and the sapphire substrate [23, 82]. When the sample cools to room temperature post-growth, the substrate and the film contract at different rates, leading to tensile strain in the WS_2 monolayer [23]. This is generally quite inhomogeneous across the sample leading to a distribution of bond lengths and a broadening of associated Raman phonon modes [81]. The FWHM values for the E^1_{2g} and A_{1g} Raman peaks are experimentally indistinguishable in the pre-transferred and post-transferred WS_2 providing further evidence that the film quality is preserved.

In Fig. 9c the PL spectra of the pre- and post-transferred WS_2 have been superimposed (plotted as absolute PL intensities) to show that there is minimal

change in peak position, but an increase in peak intensity on the Si/SiO_2 substrate. The latter is attributed to substrate enhancement effects [79, 83, 84]. In Fig. 9d Gaussian fitting has been used to separate the PL spectra into exciton and trion components. The exciton peak positions for the pre- and post-transferred WS_2 film remain the same at 2.015 eV, while its FWHM narrows very slightly from 51 meV pre-transfer to 50 meV post-transfer.

As sapphire is an insulator it cannot be used to realise a back-gate electrode when fabricating electronic devices due to the absence of a gate dielectric e.g. SiO_2. Top gated devices using ionic liquids have been demonstrated by Ponomarev et al. [85], but these are not scalable to industrial production methods as the ionic liquid is applied by hand. However, we have shown that our CVD-grown WS_2 is easy to transfer from the sapphire growth substrate to an Si/SiO_2 target substrate using a polystyrene support layer. Moreover, both Raman and PL measurements on transferred films show no sign of degradation; indeed, a small reduction of the FWHM of the 325 cm^{-1} Raman peak shows a slight narrowing, possibly due to the relaxation of stress incorporated during growth.

Finally, we believe that these advances in the rapid turnaround, large-area synthesis of monolayer WS_2 can enable future developments in high-yield fabrication processes for devices such as narrow-channel transistors [86, 87] and more advanced van der Waals heterostructure multi-quantum-well (MQW) light-emitting diodes, such as those demonstrated by Withers et al. [88]. Our CVD WS_2 recipe could also potentially be combined with established MoS_2 and graphene recipes to grow van der Waals heterostructures *in-situ* which would mean that only one transfer step would be needed onto a suitable substrate. In addition, we have shown that our optimised CVD growth recipe for WS_2 also works on Si/SiO_2 substrates eliminating the need for transfer altogether. However, these WS_2 films exhibit significantly worse optical quality (See supplementary materials, Fig. S2).

Conclusions

In conclusion, we have developed a protocol for growing uniform, large-area monolayer WS_2 films using a commercial cold-wall gas-phase CVD reactor

with a WCl_6 precursor. Exploiting our precise control over gas flow rates, we have systematically investigated the influence that post-growth annealing in different H_2S flow rates has on the quality of the WS_2 layers. For an optimal H_2S flow rate of 20sccm these studies reveal a dramatic improvement in the optical quality of our films as characterised by Raman and PL spectroscopy. Our optimally annealed material is comparable in quality with that produced by other CVD approaches reported in the literature, exhibiting intense PL exciton emission peaks centred on 2.01 ± 0.01 eV with full width at half maximum of 51 ± 2 meV. Finally, we have demonstrated that we can easily transfer our films from the sapphire growth substrate to target Si/SiO_2 substrates using a polystyrene support layer. Post-transfer Raman and PL measurements reveal no degradation in the film optical quality and show evidence of the relaxation of stress that has been incorporated during growth. Our approach is promising for future industrial-scale production of monolayer WS_2 for applications in photovoltaics, photodetectors and transistors.

Declaration

References

[1] Mak KF, Lee C, Hone J et al (2010) Atomically thin MoS_2: a new direct-gap semiconductor. Phys Rev Lett, 105. https://doi.org/10.1103/PhysRevLett.105.136805

[2] Cheiwchanchamnangij T, Lambrecht WRL (2012) Quasiparticle band structure calculation of monolayer, bilayer, and bulk MoS_2. Phys Rev B 85. https://doi.org/10.1103/PhysRevB.85.205302

[3] Lebègue S, Eriksson O (2009) Electronic structure of two-dimensional crystals from ab initio theory. Phys Rev B Condens Matter Mater Phys, 79. https://doi.org/10.1103/PhysRevB.79.115409

[4] Gusakova J, Wang X, Shiau LL et al (2017) Electronic properties of bulk and monolayer TMDs: theoretical study within DFT framework (GVJ-2e Method). Phys Status Solidi Appl Mater Sci, 214. https://doi.org/10.1002/pssa.201700218

[5] Ramasubramaniam A (2012) Large excitonic effects in monolayers of molybdenum and tungsten dichalcogenides. Phys Rev B Condens Matter Mater Phys, 86. https://doi.org/10.1103/PhysRevB.86.115409

[6] Wang L, Kutana A, Yakobson BI (2014) Many-body and spin-orbit effects on direct-indirect band gap transition of strained monolayer MoS_2 and WS_2. Ann Phys, 526. https://doi.org/10.1002/andp.201400098

[7] McCreary KM, Hanbicki AT, Jernigan GG et al (2016) Synthesis of large-area WS_2 monolayers with exceptional photoluminescence. Sci Rep, 6. https://doi.org/10.1038/srep19159

[8] Gutiérrez HR, Perea-López N, Elías AL et al (2013) Extraordinary room-temperature photoluminescence in triangular WS_2 monolayers. Nano Lett, 13. https://doi.org/10.1021/nl3026357

[9] Zhao W, Ghorannevis Z, Amara KK et al (2013) Lattice dynamics in mono- and few-layer sheets of WS_2 and WSe_2. Nanoscale, 5. https://doi.org/10.1039/c3nr03052k

[10] Yang W, Shang J, Wang J et al (2016) Electrically tunable valley-light emitting diode (vLED) based on CVD-Grown Monolayer WS_2. Nano Lett, 16. https://doi.org/10.1021/acs.nanolett.5b04066

[11] Sheng Y, Chen T, Lu Y et al (2019) High-performance WS_2 monolayer light-emitting tunneling devices using 2D materials grown by chemical vapor deposition. ACS Nano 13:4530–4537. https://doi.org/10.1021/acsnano.9b00211

[12] Eftekhari A (2017) Tungsten dichalcogenides (WS_2, WSe_2, and WTe_2): Materials chemistry and applications. J Mater Chem A 5. https://doi.org/10.1039/C7TA04268J

[13] Zeng L, Tao L, Tang C et al (2016) High-responsivity UV-Vis photodetector based on transferable WS_2 film deposited by magnetron sputtering. Sci Rep 6:20343. https://doi.org/10.1038/srep20343

[14] Lan C, Li C, Wang S et al (2017) Highly responsive and broadband photodetectors based on WS_2–graphene van der Waals epitaxial heterostructures. J Mater Chem C 5:1494–1500. https://doi.org/10.1039/C6TC05037A

[15] Cong C, Shang J, Wang Y, Yu T (2018) Optical properties of 2D semiconductor WS_2. Adv Opt Mater 6:1700767. https://doi.org/10.1002/adom.201700767

[16] Schaibley JR, Yu H, Clark G, et al (2016) Valleytronics in 2D materials. Nat Rev Mater 1. https://doi.org/10.1038/natrevmats.2016.55

[17] Cui Y, Xin R, Yu Z et al (2015) High-performance monolayer WS_2 field-effect transistors on high-κ dielectrics. Adv Mater 27:5230–5234. https://doi.org/10.1002/adma.201502222

[18] Iqbal MW, Iqbal MZ, Khan MF et al (2016) Tailoring the electrical and photo-electrical properties of a WS_2 field effect transistor by selective n-type chemical doping. RSC Adv, 6. https://doi.org/10.1039/c6ra02390h

[19] Iqbal MW, Iqbal MZ, Khan MF et al (2015) High-mobility and air-stable single-layer WS_2 field-effect transistors

sandwiched between chemical vapor deposition-grown hexagonal BN films. Sci Rep, 5. https://doi.org/10.1038/srep10699

[20] Reale F, Palczynski P, Amit I et al (2017) High-mobility and high-optical quality atomically thin WS_2. Sci Rep, 7. https://doi.org/10.1038/s41598-017-14928-2

[21] Fu Q, Wang W, Yang L et al (2015) Controllable synthesis of high quality monolayer WS_2 on a SiO_2/Si substrate by chemical vapor deposition. RSC Adv, 5. https://doi.org/10.1039/c5ra00210a

[22] Liu P, Luo T, Xing J et al (2017) Large-Area WS_2 film with big single domains grown by chemical vapor deposition. Nanoscale Res Lett, 12. https://doi.org/10.1186/s11671-017-2329-9

[23] McCreary KM, Hanbicki AT, Singh S et al (2016) The effect of preparation conditions on raman and photoluminescence of monolayer WS_2. Sci Rep, 6. https://doi.org/10.1038/srep35154

[24] Baek SH, Choi Y, Choi W (2015) Large-area growth of uniform single-layer MoS_2 thin films by chemical vapor deposition. Nanoscale Res Lett, 10. https://doi.org/10.1186/s11671-015-1094-x

[25] Lee Y-H, Zhang X-Q, Zhang W et al (2012) Synthesis of large-area MoS_2 atomic layers with chemical vapor deposition. Adv Mater 24:2320–2325. https://doi.org/10.1002/adma.201104798

[26] Park J, Lee W, Choi T et al (2015) Layer-modulated synthesis of uniform tungsten disulfide nanosheet using gas-phase precursors. Nanoscale, 7. https://doi.org/10.1039/c4nr04292a

[27] Choudhury TH, Simchi H, Boichot R et al (2018) Chalcogen precursor effect on cold-wall gas-source chemical vapor deposition growth of WS_2. Cryst Growth Des 18:4357–4364. https://doi.org/10.1021/acs.cgd.8b00306

[28] Bianco GV, Losurdo M, Giangregorio MM et al (2015) Direct epitaxial CVD synthesis of tungsten disulfide on epitaxial and CVD graphene. RSC Adv 5. https://doi.org/10.1039/c5ra19698a

[29] Yang Z, Gao D, Zhang J et al (2015) Realization of high Curie temperature ferromagnetism in atomically thin MoS_2 and WS_2 nanosheets with uniform and flower-like morphology. Nanoscale 7. https://doi.org/10.1039/c4nr06141a

[30] Cun H, Macha M, Kim HK et al (2019) Wafer-scale MOCVD growth of monolayer MoS_2 on sapphire and SiO_2. Nano Res 12. https://doi.org/10.1007/s12274-019-2502-9

[31] Krisyuk VV, Koretskaya TP, Turgambaeva AE et al (2015) Thermal decomposition of tungsten hexacarbonyl: CVD of W-containing films under Pd codeposition and VUV assistance. Phys Status Solidi Curr Top Solid State Phys 12. https://doi.org/10.1002/pssc.201510020

[32] Reale F, Sharda K, Mattevi C (2016) From bulk crystals to atomically thin layers of group VI-transition metal dichalcogenides vapour phase synthesis. Appl Mater Today 3. https://doi.org/10.1038/s41598-017-14928-2

[33] Kodas TT, Hampden-Smith MJ (2007) The chemistry of metal CVD. https://doi.org/10.1002/9783527615858.ch9

[34] Kang K, Xie S, Huang L et al (2015) High-mobility three-atom-thick semiconducting films with wafer-scale homogeneity. Nature 520. https://doi.org/10.1038/nature14417

[35] Zhang X, Al Balushi ZY, Zhang F et al (2016) Influence of carbon in metalorganic chemical vapor deposition of few-layer WSe_2 thin films. J Electron Mater 45:6273–6279. https://doi.org/10.1007/s11664-016-5033-0

[36] Okada M, Sawazaki T, Watanabe K et al (2014) Direct chemical vapor deposition growth of WS_2 atomic layers on hexagonal boron nitride. ACS Nano 8. https://doi.org/10.1021/nn503093k

[37] Okada M, Okada N, Chang WH et al (2019) Gas-Source CVD Growth of Atomic Layered WS_2 from WF_6 and H_2S Precursors with High Grain Size Uniformity. Sci Rep 9. https://doi.org/10.1038/s41598-019-54049-6

[38] Groven B, Claes D, Nalin Mehta A et al (2019) Chemical vapor deposition of monolayer-thin WS_2 crystals from the WF_6 and H_2S precursors at low deposition temperature. J Chem Phys 150:104703. https://doi.org/10.1063/1.5048346

[39] Stranks SD, Snaith HJ (2015) Metal-halide perovskites for photovoltaic and light-emitting devices. Nat Nanotechnol 10. https://doi.org/10.1038/nnano.2015.90

[40] Faehnrich HJ, Rasch E (1988) Electronic ballasts for metal halide lamps. J Illum Eng Soc 17. https://doi.org/10.1080/00994480.1988.10748733

[41] Dalla Costa MA, Alonso JM, Mranda JC et al (2008) A single-stage high-power-factor electronic ballast based on integrated buck flyback converter to supply metal halide lamps. IEEE Trans Ind Electron 55. https://doi.org/10.1109/TIE.2007.909729

[42] Li X, Li X, Zang X et al (2015) Role of hydrogen in the chemical vapor deposition growth of MoS_2 atomic layers. Nanoscale 7. https://doi.org/10.1039/c5nr00904a

[43] Kang KN, Godin K, Yang EH (2015) The growth scale and kinetics of WS_2 monolayers under varying H2 concentration. Sci Rep 5. https://doi.org/10.1038/srep13205

[44] Ammerlaan JAM, Boogaard DRM, van der Put PJ, Schoonman J (1991) Chemical vapour deposition of tungsten by H_2 reduction of WCl_6. Appl Surf Sci 53. https://doi.org/10.1016/0169-4332(91)90237-E

[45] Dumcenco D, Ovchinnikov D, Marinov K et al (2015) Large-area epitaxial monolayer MoS_2. ACS Nano 9. https://doi.org/10.1021/acsnano.5b01281

[46] Berkdemir A, Gutiérrez HR, Botello-Méndez AR et al (2013) Identification of individual and few layers of WS_2 using Raman Spectroscopy. Sci Rep 3. https://doi.org/10.1038/srep01755

[47] Wang Y, Qi L, Shen L, Wu Y (2016) Surface defect passivation of MoS_2 by sulfur, selenium, and tellurium. J Appl Phys 119. https://doi.org/10.1063/1.4946840

[48] Liang L, Meunier V (2014) First-principles Raman spectra of MoS_2, WS_2 and their heterostructures. Nanoscale 6. https://doi.org/10.1039/c3nr06906k

[49] Qiao S, Yang H, Bai Z et al (2017) Identifying the number of WS_2 layers via Raman and photoluminescence spectrum. https://doi.org/10.2991/icmmcce-17.2017.247

[50] McCreary A, Berkdemir A, Wang J et al (2016) Distinct photoluminescence and Raman spectroscopy signatures for identifying highly crystalline WS_2 monolayers produced by different growth methods. J Mater Res 31. https://doi.org/10.1557/jmr.2016.47

[51] Cadiz F, Courtade E, Robert C et al (2017) Excitonic linewidth approaching the homogeneous limit in MoS_2-based van der Waals heterostructures. Phys Rev X 7. https://doi.org/10.1103/PhysRevX.7.021026

[52] Chee SS, Oh C, Son M et al (2017) Sulfur vacancy-induced reversible doping of transition metal disulfides: Via hydrazine treatment. Nanoscale 9. https://doi.org/10.1039/c7nr01883e

[53] Sayers CJ, Farrar LS, Bending SJ et al (2020) Correlation between crystal purity and the charge density wave in 1T-VSe_2. Phys Rev Mater 4. https://doi.org/10.1103/PhysRevMaterials.4.025002

[54] Chaki S, Agarwal A (2008) Electrical properties and surface microtopographic studies of tungsten disulfide single crystals grown by CVT technique. In: Synthesis and Reactivity in Inorganic, Metal-Organic and Nano-Metal Chemistry

[55] Lin Z, Carvalho BR, Kahn E, et al (2016) Defect engineering of two-dimensional transition metal dichalcogenides. 2D Mater 3. https://doi.org/10.1088/2053-1583/3/2/022002

[56] Li L, Long R, Bertolini T, Prezhdo OV (2017) Sulfur adatom and vacancy accelerate charge recombination in MoS_2 but by different mechanisms: time-domain ab initio analysis. Nano Lett 17. https://doi.org/10.1021/acs.nanolett.7b04374

[57] Lu H, Kummel A, Robertson J (2018) Passivating the sulfur vacancy in monolayer MoS_2. APL Mater 6. https://doi.org/10.1063/1.5030737

[58] Cadot S, Renault O, Rouchon D et al (2017) Low-temperature and scalable CVD route to WS_2 monolayers on SiO_2/Si substrates. J Vac Sci Technol A Vacuum Surfaces Film 35:061502. https://doi.org/10.1116/1.4996550

[59] Mattinen M, Hatanpää T, King PJ et al (2019) Crystalline tungsten sulfide thin films by atomic layer deposition and mild annealing. J Vac Sci Technol A 37. https://doi.org/10.1116/1.5074153

[60] Wang H, Ng SM, Wong HF et al (2018) Effect of post-annealing on laser-ablation deposited WS_2 thin films. Vacuum 152. https://doi.org/10.1016/j.vacuum.2018.03.024

[61] Cwik S, Mitoraj D, Mendoza Reyes O et al (2018) Direct growth of MoS_2 and WS_2 layers by metal organic chemical vapor deposition. Adv Mater Interfaces 5. https://doi.org/10.1002/admi.201800140

[62] Lee C, Jeong BG, Yun SJ et al (2018) Unveiling defect-related raman mode of monolayer WS_2 via tip-enhanced resonance Raman scattering. ACS Nano 12. https://doi.org/10.1021/acsnano.8b04265

[63] Ren DD, Qin JK, Li Y et al (2018) Photoluminescence inhomogeneity and excitons in CVD-grown monolayer WS_2. Opt Mater (Amst) 80. https://doi.org/10.1016/j.optmat.2018.04.043

[64] Tongay S, Suh J, Ataca C et al (2013) Defects activated photoluminescence in two-dimensional semiconductors: Interplay between bound, charged, and free excitons. Sci Rep 3. https://doi.org/10.1038/srep02657

[65] Sercombe D, Schwarz S, Del P-Z et al (2013) Optical investigation of the natural electron doping in thin MoS_2 films deposited on dielectric substrates. Sci Rep 3. https://doi.org/10.1038/srep03489

[66] Mouri S, Miyauchi Y, Matsuda K (2013) Tunable photoluminescence of monolayer MoS_2 via chemical doping. Nano Lett 13. https://doi.org/10.1021/nl403036h

[67] Amani M, Lien DH, Kiriya D et al (2015) Near-unity photoluminescence quantum yield in MoS_2. Science 80:350. https://doi.org/10.1126/science.aad2114

[68] Wang H, Zhang C, Rana F (2015) Ultrafast dynamics of defect-assisted electron-hole recombination in monolayer MoS_2. Nano Lett 15. https://doi.org/10.1021/nl503636c

[69] Yuan L, Huang L (2015) Exciton dynamics and annihilation in WS_2 2D semiconductors. Nanoscale 7. https://doi.org/10.1039/c5nr00383k

[70] Cohen A, Patsha A, Mohapatra PK, et al (2020) Growth-Etch metal–organic chemical vapor deposition approach of WS_2 atomic layers. ACS Nano acsnano.0c05394. https://doi.org/10.1021/acsnano.0c05394

[71] Andrzejewski D, Myja H, Heuken M et al (2019) Scalable large-area p-i-n light-emitting diodes based on WS_2 monolayers grown via MOCVD. ACS Photonics 6. https://doi.org/10.1021/acsphotonics.9b00311

[72] Xu Z, Lv Y, Li J et al (2019) CVD controlled growth of large-scale WS_2 monolayers. RSC Adv 9. https://doi.org/10.1039/c9ra06219j

[73] Kobayashi Y, Sasaki S, Mori S et al (2015) Growth and optical properties of high-quality monolayer WS_2 on

graphite. ACS Nano 9. https://doi.org/10.1021/acsnano.5b00103

[74] Yorulmaz B, Özden A, Şar H et al (2019) CVD growth of monolayer WS₂ through controlled seed formation and vapor density. Mater Sci Semicond Process 93. https://doi.org/10.1016/j.mssp.2018.12.035

[75] Sheng Y, Tan H, Wang X, Warner JH (2017) Hydrogen Addition for Centimeter-Sized Monolayer Tungsten Disulfide Continuous Films by Ambient Pressure Chemical Vapor Deposition. Chem Mater 29. https://doi.org/10.1021/acs.chemmater.7b00954

[76] Irisawa T, Okada N, Mizubayashi W et al (2018) CVD growth technologies of layered MX₂ materials for real LSI applications - position and growth direction control and gas source synthesis. IEEE J Electron Devices Soc 6. https://doi.org/10.1109/JEDS.2018.2870893

[77] Choi W, Choudhary N, Han GH et al (2017) Recent development of two-dimensional transition metal dichalcogenides and their applications. Mater Today 20. https://doi.org/10.1016/j.mattod.2016.10.002

[78] Wang QH, Kalantar-Zadeh K, Kis A, et al (2012) Electronics and optoelectronics of two-dimensional transition metal dichalcogenides. Nat Nanotechnol 7. https://doi.org/10.1038/nnano.2012.193

[79] Gurarslan A, Yu Y, Su L et al (2014) Surface-energy-assisted perfect transfer of centimeter-scale monolayer and few-layer MoS₂ films onto arbitrary substrates. ACS Nano 8. https://doi.org/10.1021/nn5057673

[80] Ma D, Shi J, Ji Q et al (2015) A universal etching-free transfer of MoS₂ films for applications in photodetectors. Nano Res 8:3662–3672. https://doi.org/10.1007/s12274-015-0866-z

[81] Dadgar AM, Scullion D, Kang K et al (2018) Strain engineering and Raman spectroscopy of monolayer transition metal dichalcogenides. Chem Mater 30. https://doi.org/10.1021/acs.chemmater.8b01672

[82] Kumar P, Singh B, Kumar P, Balakrishnan V (2018) Competing thermal expansion mismatch and lattice strain engineered growth of crack free WS₂ in-plane heterostructures. J Mater Chem C 6. https://doi.org/10.1039/c8tc04573a

[83] Buscema M, Steele GA, van der Zant HSJ, Castellanos-Gomez A (2014) The effect of the substrate on the Raman and photoluminescence emission of single-layer MoS₂. Nano Res 7. https://doi.org/10.1007/s12274-014-0424-0

[84] Li SL, Miyazaki H, Song H et al (2012) Quantitative raman spectrum and reliable thickness identification for atomic layers on insulating substrates. ACS Nano 6. https://doi.org/10.1021/nn3025173

[85] Ponomarev E, Gutiérrez-Lezama I, Ubrig N, Morpurgo AF (2015) Ambipolar light-emitting transistors on chemical vapor deposited monolayer MoS₂. Nano Lett 15. https://doi.org/10.1021/acs.nanolett.5b03885

[86] Schwierz F, Pezoldt J, Granzner R (2015) Two-dimensional materials and their prospects in transistor electronics. Nanoscale 7. https://doi.org/10.1039/c5nr01052g

[87] Nourbakhsh A, Zubair A, Sajjad RN et al (2016) MoS₂ field-effect transistor with Sub-10 nm channel length. Nano Lett 16. https://doi.org/10.1021/acs.nanolett.6b03999

[88] Withers F, Del Pozo-Zamudio O, Mishchenko A et al (2015) Light-emitting diodes by band-structure engineering in van der Waals heterostructures. Nat Mater 14. https://doi.org/10.1038/nmat4205

Publisher's Note Springer Nature remains neutral with regard to jurisdictional claims in published maps and institutional affiliations.